High-resolution and extended-depth-of-field photoacoustic endomicroscopy by scanning-domain synthesis of optical beams

XIN JIN,[1,2] XINKUN WANG,[2] KEDI XIONG,[1,2,3] AND SIHUA YANG[1,2,4]

[1]*MOE Key Laboratory of Laser Life Science & Institute of Laser Life Science, South China Normal University, Guangzhou 510631, China*
[2]*College of Biophotonics, South China Normal University, Guangzhou 510631, China*
[3]*xiongkd2012@163.com*
[4]*yangsh@scnu.edu.cn*

Abstract: Photoacoustic endomicroscopy (PAEM) is capable of imaging fine structures in digestive tract. However, conventional PAEM employs a tightly focused laser beam to irradiate the object, which results in a limited depth-of-field (DOF). Here, we propose a scanning-domain synthesis of optical beams (SDSOB) to optimize both transverse resolution and the DOF by synthetic effective focused beams in scanning domain for the PAEM. By utilizing the SDSOB technique, multiple defocused and scattered beams are refocused to synthesize virtual focuses covering a large range of depth. A transverse point spread function that is 5.7-time sharper, and a transverse spatial bandwidth that is 8.5-time broader than those of the conventional PAEM were simulatively obtained through SDSOB-PAEM at the defocus distance of 2.4 mm. We validated the transverse resolution improvement at both in- and out-focus positions via phantom experiments of carbon fibers. In addition, *in vivo* rabbit experiments were conducted to acquire vascular images over radial depth range of 900 μm. And further morphological analysis revealed that the SDSOB images were acquired with abundant vascular branches and nodes, large total-length and small average-length of blood vessels, which indicated that the SDSOB-PAEM achieved high-resolution imaging in distinct rectal layers. All these results suggest that the SDSOB-PAEM possesses high transverse resolution and extended DOF, which demonstrates the SDSOB-PAEM can provide more accurate information for clinical assessment.

1. Introduction

As a novel imaging method [1–4], photoacoustic (PA) imaging has been developing rapidly driven by features with optical absorption contrast, high spatial resolution, and the potential of functional imaging [5,6]. The PA imaging mainly contains PA microscopy [7–9] that provides a high transverse resolution and PA endoscopy (PAE) [10–15] that employs a miniaturized probe to image internal organs. Photoacoustic endomicroscopy (PAEM) achieves a microscale PA imaging in endoscope, which enables internal organ imaging with a much finer resolution than conventional PAE. The PAEM has been widely applied for various applications due to its excellent imaging performance [16,17].

The PAEM can be achieved by optical focusing or acoustic focusing, correspondingly termed as optical-resolution PAEM [18,19] and acoustic-resolution PAEM [20,21]. Optical focusing tends to provide higher transverse resolution than acoustic focusing, thus the PAEM is generally based on a tightly focusing of high numerical aperture (NA). However, due to the tradeoff between NA and depth of focus [22], objective lens with high NA results in a short focal depth. Although, a small-aperture objective lens is desired for implementation of a miniature probe which is easier to pass through the endoscopic channel in clinical applications or reduce the pain of patients, but the short working distances of miniaturized endoscopic probes using the combination of

a gradient index lens and a single-mode optical fiber limit the application in a large cavity [23]. Bessel beams have been used for depth-of-focus extension, which can maintain a high transverse resolution over a depth of focus larger than the Rayleigh distance [24,25]. However, compared to Gaussian beams, the coherent transfer functions of the Bessel beams suffer a major loss of spatial frequency components, resulting in sidelobe artifacts and a significant decline of sensitivity [26]. Although autofocusing with a liquid lens obtains a good transverse resolution on the mucosal surface [27], the transverse resolution deteriorates rapidly in deep tissue due to high scattering properties of biological tissue. Synthetic aperture focusing technique (SAFT, is a method that can restore the degraded transverse resolution in the defocused region and the scattered tissue) has been reported in forward-viewing and side-viewing acoustic-resolution PA endoscopes [28,29]. The SAFT generally employs a large-view-angle laser illumination and a focused ultrasonic detection of large NA to acquire high-transverse-resolution PA imaging [30,31]. However, SAFT-PAEM based on acoustic beam synthesis provides a lower resolution compared with the conventional optical-resolution PAEM. A higher transverse resolution can be obtained by a synthesis of multiple optical beams for the PAEM in comparison with the conventional optical-resolution PAEM.

In this work, we proposed a scanning-domain synthesis of optical beams (SDSOB) for the PAEM with opto-sono confocal scanning, which simultaneously achieved excellent resolution, high contrast and large depth of field (DOF). Tightly focused beam by large-NA objective ensures a wide aperture angle and thus a large overlap of scanning beams. Numerical analysis and subsequent phantom experiments proved that the SDSOB effectively extended optical DOF and improved the transverse resolution in focus and out-of-focus regions. *In vivo* imaging experiments further exhibited that SDSOB-PAEM achieved high-resolution microvascular imaging of irregular rectal mucosa, meanwhile realized high-analytical vascular images in distinct layers, which demonstrated the feasibility and efficacy of high-resolution biological tissue imaging with a dramatic DOF extension.

2. Methods

2.1. Photoacoustic endomicroscopy system

Figure 1(a) shows the schematic of the PAEM system. The source provides a pulse laser with wavelength of 532 nm, pulse width of ~7 ns, and repetition rate of 8-kHz. The transmission pulses are simultaneously monitored by a photodiode and focused into a 30-μm-diameter pinhole for spatial filtering by Lens1. The filtered beam is then collimated by Lens2 and coupled to a single-mode fiber (SMF) via a fiber coupler (PAF-X-7-A, Thorlabs). The SMF is coupled to the probe via a proximal actuation unit (PAU). The PAU integrates fiber-electric slip ring (FESR), rotate motor (RM) and linear motor (LM), and the RM and LM are actuated by an external motor driver to control the probe for rotation and linear motion. The proximal end of the probe is fixed on the rotor of the FESR, by which inside the probe, the optical transmission, as well as signal transmission, are realized. Hence, under the actuating of the RM, the probe and the rotor of the FESR rotate synchronously during scanning. Meanwhile, the LM is exploited to move the probe forward or backward for 3D scanning. The dashed box in Fig. 1(a) indicates the probe housing with an outer diameter of 5 mm. The laser beam is collimated and focused by aspherical lenses AL1 and AL2 inside the probe. The focused optical beam passes through the center circular hole of the ultrasonic transducer (UT) through the 45° reflecting prism to the tissue surface. The UT is a ring focused ultrasonic transducer with an outer diameter of 3 mm and an inner diameter of 1.2 mm, and its surface is tangent to the probe housing. The center frequency, bandwidth, and focal length of the UT are 15 MHz, 92%, and 5.5 mm, respectively. The PA signal is amplified by 50 dB and recorded by DAS with sampling rate of 100 MS/s, and then transmitted to computer for reconstruction and display.
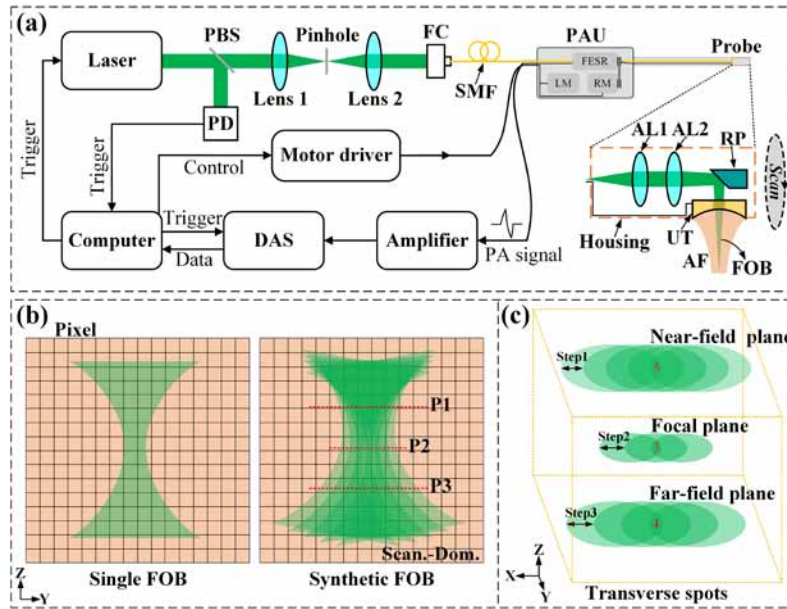
Fig. 1. (a) Schematic of the PAEM system. PBS, polarizing beam splitter; PD, photodiode; FC, fiber coupler; SMF, single-mode fiber; PAU, proximal actuation unit; FESR, fiber-electric slip ring; LM, linear motor; RM, rotate motor; AL, aspherical lens; RP, reflecting prism; UT, ultrasound transducer; AF, acoustic field; FOB, focused optical beam; DAS, data acquisition system. (b) Single FOB in the conventional PAEM system vs. synthetic FOB in the SDSOB-PAEM system. Scan.-Dom., scanning-domain; P1, P2, P3 transverse planes, at different positions, of the synthetic FOB. (c) Transverse spots of the synthetic FOB corresponding to P1, P2, P3, respectively.

2.2. *Scanning-domain synthesis of optical beams*

Note that the conventional PAEM uses a single focused optical beam (FOB) to irradiate the tissue. As shown in Fig. 1(b), the depth of focus and focal-spot size of a single FOB are limited by its physical beam shape, which is mainly determined by the wavelength and the NA of optical system. In consequence, the transverse resolution and the DOF are limited.

Instead of using a single FOB, the SDSOB (as shown in Fig. 1(b and c)) adopts multiple successive beams to synthesize virtual focuses covering a large depth range in scanning domain. A synthetic FOB with a sharper focus and an extended focal depth can be realized by generating scanning-coded multiple beams at lateral regions. The effective overlap of scanning-domain transverse spots ensures the synthesis of optical beams (Fig. 1(c)). In the SDSOB approach, the minimum variance (MV) optimization criteria [32–34] is applied to acquire optimal weights that encode the scanning-domain optical beams, which is employed to obtain the high-resolution synthetic FOB via superposing these scanning-coded beams. Physically, The SDSOB-PAEM system can be regarded as an incoherent optical system that satisfies the principle of intensity superposition. It should be pointed out that the SDSOB-PAEM system includes optical excitation and acoustic receiving system, and it is still coherent for the acoustic receiving system. Hence, the point spread function (PSF) of the synthetic FOB can be calculated as

$$h_I^{SDSOB} = \mathbf{W}^{\mathrm{T}}\mathbf{H} = \sum_{i=1}^{N} w_i \cdot h_I^i, \tag{1}$$

where h_I^{SDSOB} is the synthetic PSF, $\mathbf{W}$ is the weight vector for the PSFs of the scanning-domain optical beams and $\mathbf{W} = [w_1, w_2, \dots, w_N]^T$, and $\mathbf{H}$ is the PSFs of the scanning-domain beams which are selected for synthesis and $\mathbf{H} = [h_I^1, h_I^2, \dots, h_I^N]^T$. The output of Eq. (1) is a weighted sum of the optical beam spatial intensity (Usually, it is normalized intensity) in scanning domain which is determined by the geometry and scanning of the optical beams. The MV optimization principle ensures that the power of the synthetic FOB is minimized, meanwhile maintaining unit gain on the optical axis of the synthesis FOB and suppressing off-axis intensity, which leads to a much narrower full width at half-maximum (FWHM) for h_I^{SDSOB} than the PSF of the single FOB. Note that the SDSOB approach is implemented to gain an array of optimal weights in post-processing since these scanning-domain beams are not at the same time. Mathematics is expressed as

$$\min[\mathbf{W}^T\mathbf{R}\mathbf{W}], \text{subject to } \mathbf{W}\alpha = 1, \tag{2}$$

where α is the steering vector for the scanning-domain optical beams, and $\mathbf{R}$ is the covariance matrix expressed as

$$\mathbf{R} = E[\mathbf{H}\mathbf{H}^T] = \frac{1}{N}\sum_{i=1}^{N}\mathbf{H}\mathbf{H}^T. \tag{3}$$

The optimal weights $\mathbf{W}_{SDSOB}$ can be obtained through seeking the constrained optimization problem of Eq. (2) by the Lagrangian multiplier theory as

$$\mathbf{W}_{SDSOB} = \frac{\mathbf{R}^{-1}\alpha}{\alpha^T\mathbf{R}^{-1}\alpha}. \tag{4}$$

Applying the weights $\mathbf{W}_{SDSOB}$ to Eq. (1) gives the optimal h_I^{SDSOB} (the synthetic PSF, that characterizes the spatial intensity distribution of the synthetic FOB) based on the MV principle. That is to say, the synthetic FOB achieves resolution improvement compared to the single FOB. On the other hand, the PA signals are only yielded from locations where optical absorbers are located within the field of view (FOV) of the optical beams since the width of the optical beams is narrower than that of the acoustic field. Thus, the PSF of the optical beam determines the resolution of the PA signals. That is, the PSF of the single FOB determines the resolution of the conventional PAEM system and the PSF of the synthetic FOB determines the resolution of the SDSOB-PAEM system. The broad PSF of the defocused beam will cause blurred data and the sharp PSF of the synthetic beam will lead to high-resolution data. The PA signals can be simply described by

$$P = \mu\Gamma I, \tag{5}$$

where P is the amplitude of the PA signals. μ is the optical absorption coefficient. For simplicity, we consider a constant and uniform optical absorption distribution. Γ represents Grüneisen parameter which is considered to be a constant. I is the intensity of exciting optical beams. As shown in Eq. (5), the PA signals are proportional to the optical beam intensity. Consequently, the $\mathbf{W}_{SDSOB}$ is also applicable to the PA signals. A number of adjacent scanning lines (A-lines) are selected to receive PA signals (PA1, PA2, PA3, . . .), which are indicated by blue dotted lines in Fig. 2(a). For the ith optical beam (Fig. 2(b)), the intensity of the PSF at the imaging target is $h_I^i(\Delta, r)$, where Δ is the defocus distance and r is the distance from the imaging target to the optic axis. Note, the PSF is split to separately account in the lateral dimension owing to scanning step (Fig. 2(b)). The received PA data on the A-line contain a summation of PA signals which have the same spatial distance to the ultrasound transducer. Usually, the distance from the imaging target to the ultrasound transducer is much larger than the transverse spot size at the imaging target. Therefore, the discrete accounts of the PSF can be regarded as equidistant to the

ultrasound transducer. The ith PA signal P_{targ} at the imaging target can be computed as

$$P_{targ} = \mathrm{N\_}h_I^i \cdot P_i(t - \tau_i), \tag{6}$$

where $P_i(t)$ is the ith PA signal and τ_i is the time delay for $P_i(t)$. $\mathrm{N\_}h_I{}^i$ represents normalized transverse PSF of the ith optical beam and is given by

$$\mathrm{N\_}h_I^i = \frac{h_I^i(\Delta, r)}{\sum\limits_k h_I^i(\Delta, r_k)}, \tag{7}$$

where $\sum h_I{}^i(\Delta, r_k) = h_I{}^i(\Delta, r_1) + h_I{}^i(\Delta, r_2) + \ldots + h_I{}^i(\Delta, r_N)$. The process of the SDSOB can be expressed as

$$P_{SDSOB}(t) = \mathbf{W}_{SDSOB}^{\mathrm{T}} \mathbf{P}(t) = \sum_{i=1}^{N} w_i \cdot \mathrm{N\_}h_I^i \cdot P_i(t - \tau_i), \tag{8}$$

where $P_{SDSOB}(t)$ is the synthetic PA signal. $\mathbf{P}(t)$ is scanning-domain PA signals and $\mathbf{P}(t) = [\mathrm{N\_}h_I{}^1 \cdot P_1(t-\tau_1), \mathrm{N\_}h_I{}^2 \cdot P_2(t-\tau_2), \ldots, \mathrm{N\_}h_I{}^N \cdot P_N(t-\tau_N)]^{\mathrm{T}}$. The PA signals are synthesized to generate a high-resolution and -contrast PA signal, leading to a efficient virtual focusing shown as the yellow triangle region in Fig. 2(a). N in above Eqs. represents the number of effective overlapped optical beams, which is calculated as

$$N = L_R(\theta, R_f)/(\delta \cdot R), \tag{9}$$

where L_R is the transverse beam width at the radial distance of R. R_f is the radial distance at focus. When $R > R_f$, L_R increases as R increases; when $R < R_f$, L_R decreases as R increases. Generally, N increases as the degree of defocus increases, and has the smallest value when in the focal plane. θ is the aperture angle of the single FOB. The larger θ is, the smaller L_R in the focus region is and the larger L_R out the focus region is. Obviously large θ is conducive to the SDSOB. δ represents the step scan angle. The smaller δ is, the larger N is, the slower the scanning speed is at the same time. A large N will lead to a large synthetic aperture for the SDSOB and significantly refocusing of the A-lines out the focus region. In this study, the diameter and the focal length of AL2 are 3 mm and 9 mm, respectively, and R_f is 8.2 mm. A cross-sectional image (B-scan) contains 8000 A-lines in the simulation and phantom experiment, and 4000 A-lines in the *in vivo* rabbit experiment which needs a larger scanning speed to overcome motion artifacts.
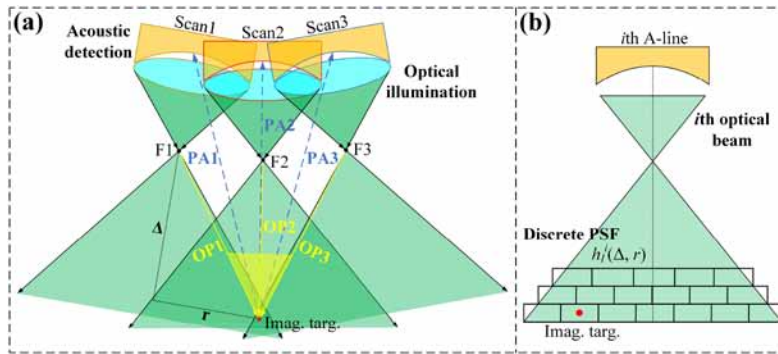

Fig. 2. Working principles of the SDSOB technique. F1, F2, F3 the focuses of optical beams; Imag. targ., imaging target; OP, optical path.

2.3. Numerical analysis

Here, we characterize the excitation FOB of the PAEM system via the PSF and the optical transfer function (OTF) [35] which are represented as $h_I(x, y)$ and $H(u, v)$, respectively. Note that $H = F(h_I)$, where $F(\cdot)$ represents the Fourier transform; (x, y) and (u, v) are coordinates in the spatial and Fourier domains, respectively. The OTFs can be calculated as autocorrelation of the pupil functions (PFs) of the objective. For simplicity, we consider the circle function as the PF [22] that is mathematically expressed as

$$p(x, y) = circ(\sqrt{x^2 + y^2}/D), \tag{10}$$

where $p(x, y)$ is the PF and D is the radius of objective aperture. Equation (10) shows that when a point (x, y) is located inside the aperture, $p(x, y) = 1$; otherwise, $p(x, y) = 0$. The PSFs can be obtained by calculating the inverse Fourier transform of the OTFs. The OTFs and PSFs are simulated according to Eqs. (1)–(4).

Numerical simulations of OTFs and PSFs of the conventional- and SDSOB-PAEM systems were performed using MATLAB software (MathWorks, Natick, Massachusetts, USA). Figures 3(a)–3(c) show the OTFs of the single and synthetic FOB in the focal plane ($\Delta=0$) and out-of-focus planes ($\Delta=1$ mm, $\Delta=2$ mm) respectively, where u is the normalized spatial frequency. Figures 3(d)–3(f) show the PSFs corresponding to the OTFs in Figs. 3(a)–3(c), respectively. The cutoff frequency of the OTF is the largest (Fig. 3(a)) and the FWHM of the PSF is the smallest (Fig. 3(d)) in
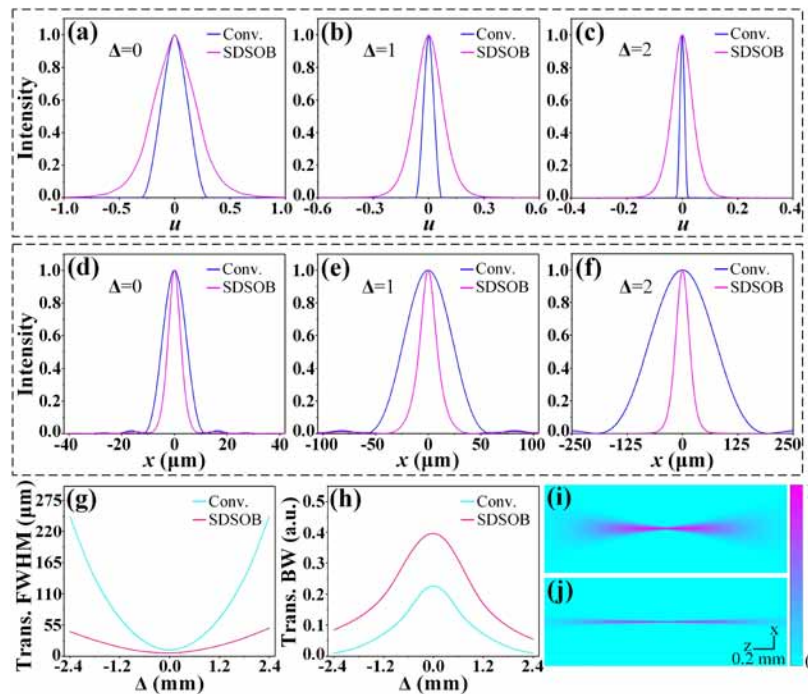

Fig. 3. Numerical simulation results. (a)–(c) Transverse optical transfer functions (OTFs) in the focal plane and at the out-of-focus planes of $\Delta=1$ mm, $\Delta=2$ mm, respectively. (d)–(f) Transverse PSFs in the focal plane and at the out-of-focus planes of $\Delta=1$ mm, $\Delta=2$ mm. (g) Transverse spot size of a single FOB and a synthetic FOB versus the radial distance. (h) Transverse bandwidth of a single FOB and a synthetic FOB versus the radial distance. (i) and (j) Two-dimension PSFs of a single FOB and a synthetic FOB over the transverse (x) and radial (z) directions.

the focal plane. As Δ increases, the cutoff frequency becomes smaller (Figs. 3(a)–3(c)) and the FWHM becomes larger (Figs. 3(d)–3(f)). The FWHMs of the synthetic FOB are smaller than those of the single FOB. As Δ increases, the FWHM of the single FOB rapidly increases, while that of the synthetic FOB remains at a lower level (Fig. 3(g)). Meanwhile, the bandwidths (BWs) of the synthetic FOB are larger than those of the single FOB. As Δ increases, the BW of the single FOB gradually decreases to near zero while the synthetic FOB can maintain a broad BW (Fig. 3(h)). The PSF, that is 5.7-time sharper, and the spatial BW, that is 8.5-time broader, of the synthetic FOB than those of the single FOB at the defocus distance of 2.4 mm. In particular, the SDSOB-PAEM has a different number of scanning-coded beams at both sides of focus with same Δ along the radial direction. According to Eq. (9), the number of scanning-coded beams at $\Delta<0$ is larger than at $\Delta>0$, thus the FWHM at $\Delta<0$ is smaller than at $\Delta>0$ (Fig. 3(g)), correspondingly, the BW at $\Delta<0$ is larger than at $\Delta>0$ (Fig. 3(h)). As shown in Figs. 3(i) and 3(j), the SDSOB is effective for the out-of-focus regions and focus regions, which greatly extends the depth of focus. The number of scanning-coded beams at larger Δ far exceeds at the focus, leading to a significant refocusing of defocused beams and improving the transverse resolution greatly over the entire radial field of view. The parameters of the single FOB and synthetic FOB, which concludes NA, focal spot size and depth of focus, are compared in Table 1. Here, we consider $NA = D/f = \tan(\theta/2)$ [22], where D is the radius of the exit aperture of the FOBs, f is the focal length of the FOBs, and θ is the aperture angle of the FOBs.

Table 1. Focusing parameters of the single FOB and synthetic FOB

	NA	Focal spot size	Depth of focus
Single FOB	0.04	23 μm	0.56 mm
Synthetic FOB	0.009	11 μm	1.88 mm

3. Experiments and results

3.1. Phantom study

Three 7 μm thick carbon fibers were inserted into agar phantom and placed at different depths (Fig. 4(a)) to evaluate the transverse resolution, at different radial distances (RDs), of the SDSOB-PAEM system. As shown in Figs. 4(a) and 4(d), O is the center of the probe, and the RD of P2, which is at the optical focus, is 8.2 mm. The RDs of P1 and P3 are 7 and 9.4 mm, respectively. The PA signal acquired by the DAS was then filtered by a digital bandpass filter with a bandwidth of 5-28 MHz to decrease electromagnetic interference and frequency spectrum aliasing. Due to defocusing of the laser beam , both P1 and P3 show significant deterioration in transverse resolution (Fig. 4(b)). Since the A-lines will become thin as the RD increases, the imaging result of P3 exhibits a wider lateral range than that of P1, while P2 maintains a good transverse resolution owing to narrow Gaussian waist (Fig. 4(b)). The SDSOB-PAEM, however, exhibits better transverse resolution over a large radial field of view (Fig. 4(e)), where the imaging results of P1, P2, and P3, compared with Fig. 4(b), demonstrate improved, nearly uniform, transverse resolution to varying degrees. Figures 4(c) and 4(f) present the original and SDSOB transverse pixel widths of the carbon fibers, respectively. Here, the transverse pixel widths were utilized as the transverse PSFs to evaluate the transverse resolution. For the original image, the transverse FWHMs of the PSFs at P1, P2, and P3 are 59, 25, and 71 μm, respectively (Fig. 4(c)). For the SDSOB image, the corresponding transverse FWHMs are 18, 11, and 19 μm, respectively (Fig. 4(f)). Obviously, smaller and more constant FWHMs are obtained in the SDSOB image. In addition, the signal-to-noise ratios (SNRs) of the SDSOB image were significantly improved. Figures 4(g) and 4(h) are original and SDSOB PA radial maximum amplitude projection (RMAP) images of the resolution panel with 10-μm line width and 30-μm pitch at the out-of-focus plane of

Δ=0.6 mm, respectively, which reveal that the original images with unresolvable targets and the SDSOB images with the targets being resolved. Figure 4(i) exhibits profiles indicated by the white dotted line in Figs. 4(g) and 4(h), demonstrating significantly improved transverse resolution in the out-of-focus region. The phantom imaging results demonstrate that the SDSOB-PAEM, in comparison with the conventional PAEM, achieves higher contrast, larger DOF and higher transverse resolution.
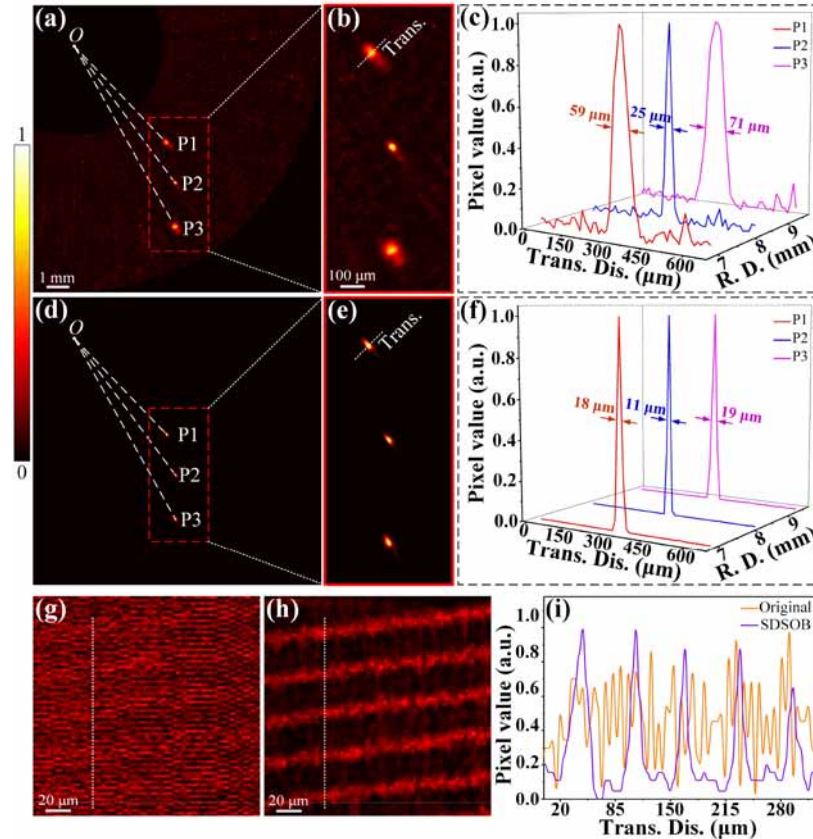

Fig. 4. Phantom imaging results. (a) and (d) Original and SDSOB PA B-scan images of the 7 μm thick carbon fibers at three different radial positions, respectively. P1 and P3 out the focal plane, P2 in the focal plane. (b) and (e) Enlarged views of the red dashed rectangles in (a) and (d), respectively. (c) and (f) Transverse pixel value of carbon fibers corresponding to (b) and (e), respectively. (g) and (h) Original and SDSOB PA radial maximum amplitude projection (RMAP) images of the resolution panel with 10-μm line width and 30-μm pitch at the out-of-focus plane of Δ=0.6 mm, respectively. (i) Pixel value on white dotted lines in (g) and (h).

3.2. In vivo rabbit study

The animal experiments were conducted under the approval of the South China Normal University (SCNU). A New Zealand rabbit (2 kg, female) was involved for *in vivo* experiments. The rabbit was firstly anesthetized with intravenous injection of 30 mg/kg sodium pentobarbital, and then a PAEM probe with a water balloon (for acoustic coupling) in the distal end was inserted into the rabbit rectum. The radius of the water balloon and the pulsed laser energy were set to 8 mm and 1.2 μJ, respectively. Figure 5 shows B-scan images of a selected rectal cross section. Figures 5(a)

and 5(d) are images by conventional- and SDSOB-PAEM, respectively. In consideration of the support of the water balloon and the uniform distribution of the rectal mucosal blood vessels, the boundary of rectal mucosa is fitted by connecting the microvessels using a dashed curve L (Fig. 5(a) and Fig. 5(d)). Figure 5(b) and Fig. 5(e) show the zoomed-in regions of interest (ROIs), which are about 400 μm beneath the rectal mucosa, indicated by white dotted box in Fig. 5(a) and Fig. 5(d), respectively. The capillaries are blurred in the original image (Fig. 5(b)) but clear in the SDSOB image (Fig. 5(e)). The SDSOB-PAEM can achieve high-resolution imaging of biological tissues via synthesizing FOBs by multiple scattered beams, despite the fact that the scattering of light beam makes the deterioration of transverse resolution more serious at such depth. The imaging results reveal that the SDSOB-PAEM can provide submucosal blood vessels images with high transverse resolution. Figures 5(c) and 5(f) exhibit profiles indicated by the white dotted line in Figs. 5(b) and 5(e), respectively, demonstrating significantly improved transverse resolution and contrast in the SDSOB image.
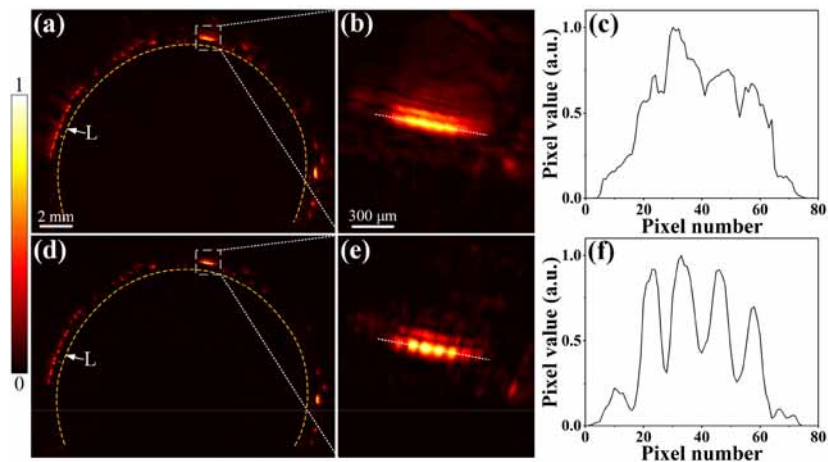

Fig. 5. *In vivo* imaging results of rabbit rectal cross section. (a) and (d) *In vivo* original and SDSOB PA B-scan images of the rabbit rectum. L the fitted curve of the rectal mucosa. (b) and (e) Zoomed-in ROIs indicated by white dotted boxes in (a) and (d), respectively. (c) and (f) Pixel value on white dotted lines in (b) and (e), respectively.

Furthermore, an arbitrarily chosen volume (900 frames B-scans, 80° field of angle-view) was rendered with the RMAP, by retracting the probe along axial direction with a speed of 20 μm/s and a step of 10 μm. Continuous cross-section images were thus obtained at 2 frames per second. Figures 6(a)–6(d) show the original- and SDSOB-RMAP images with the radial depth range of 8-8.9 mm and 8-8.3 mm respectively, which reveal the distribution of the vascular system in the coronal plane of the rabbit rectum. The acoustically coupled water balloon in the distal end of the probe was controlled to be nearly spherical to ensure that the irregular inner surface of the rectal wall was with the same radial distance, and thus the images with radial distance coding corresponded well to the distinct layers. Figures 6(a) and 6(b) show images of the full rectal layers (with a thickness of 900 μm). Figures 6(c) and 6(d) show in-focus images of the superficial layers with a thickness of 300 μm (in fact, the focused light beam is diffuse when in biological tissue, which inevitably causes resolution deterioration to extent). As can be seen from Fig. 6(a) and 6(c), the imaging of deep vessels is deteriorated severely with impaired resolution and contrast, and the imaging resolution of superficial vessels decreases slightly. Figures 6(b) and 6(d) show images with higher resolution and contrast than Figs. 6(a) and 6(c), demonstrating that the SDSOB significantly improves the resolution of images and extends the DOF.
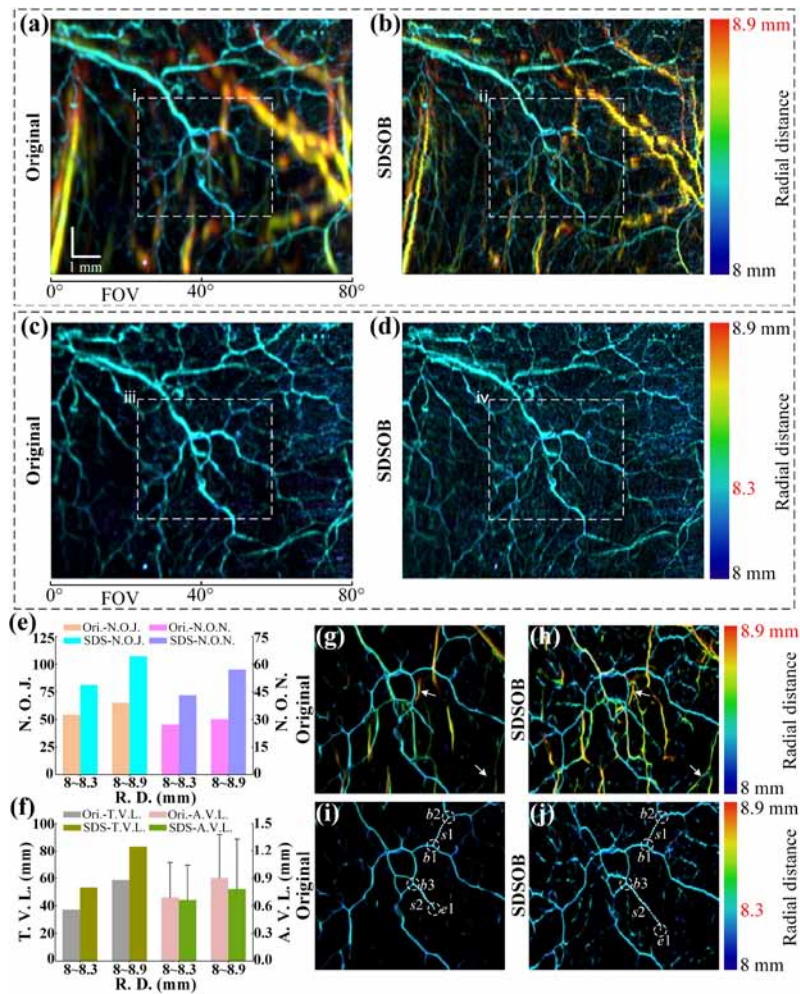
Fig. 6. *In vivo* imaging results of rabbit rectal coronal plane. (a) and (b) Original and SDSOB radial maximum amplitude projection (RMAP) images with radial distance encoding, corresponding to R.D. = 8~8.9 mm. (c) and (d) Original and SDSOB RMAP images with radial distance encoding, corresponding to R.D. = 8~8.3 mm. FOV, field of view. (e) Number of junctions (N. O. J.) and number of nodes (N. O. N.) in (g)–(j). (f) Total vessel length (T. V. L.) and average vessel length (A. V. L.) in (g)–(j). (g)–(j) The vascular tree corresponding to i, ii, iii and iv in (a)–(d), respectively.

Vascular tree images (Figs. 6(g)–6(j)) indicated by the white boxes in Figs. 6(a)–6(d) were extracted by morphological method. As indicated by the white arrows in Figs. 6(g) and 6(h), the branches of deep vessels are indistinguishable. As shown in Figs. 6(i) and 6(j), nodes and endpoints of the vascular tree were marked for quantitative analysis, where *b* was defined as the node of the blood vessel (i.e. the bifurcation point of the blood vessel), *e* the endpoint of the blood vessel, *s* the branch of the blood vessel (i.e. the blood vessel between the node and the endpoint). Figure 6(e) shows the number of blood vessel branches and blood vessel nodes in Figs. 6(g)–6(j). Figure 6(f) shows total and average length of blood vessels in Figs. 6(g)–6(j). These results reveal that, compared with the original images, the SDSOB images are acquired with more abundant vascular branches and nodes, larger total-length and less average-length of

blood vessels, verifying that the SDSOB-PAEM achieves high-resolution imaging in distinct rectal layers. Moreover, all these indexes of the full-layer image are better than those of the surface-layer image, which further indicates that the imaging sensitivity to deep vessels can be improved greatly. Comparison among the results of volumetric images demonstrates that, the SDSOB-PAEM achieves larger DOF and higher transverse resolution than the conventional PAEM, while provides more information for clinical diagnosis.

4. Discussions and conclusions

The SDSOB method is, for the first time to our knowledge, proposed for the PAEM, which demonstrates dramatic optical DOF extension performance. The SDSOB-PAEM achieves an enhanced spatial resolution and image contrast based on highly refocusing by synthesizing an effective FOB compared with the conventional optical-resolution PAEM. These merits of the SDSOB method have been validated theoretically and experimentally in this work. Numerical simulations demonstrated that the SDSOB-PAEM system achieved a sharp PSF and a broad spatial BW over a large depth of focus. Phantom experiments of carbon fibers were conducted to evaluate the performance of the SDSOB-PAEM system. And the PSF was obtained, which was in good agreement with numerical analysis, verifying that the SDSOB-PAEM owned a great resolution in both out-of-focus and focus regions. To further verify the feasibility of the SDSOB-PAEM in biological tissues, we performed *in vivo* imaging of a rabbit rectum. The results clearly visualized the vascular networks, including large vessels, small vessels, and capillaries vessels, confirming the SDSOB technique provided a sufficient DOF to stably acquire microscale resolution images *in vivo*. Here, we coherently synthesized A-lines weighted by normalized PSFs of scanning-coded beams to obtain one DOF extended A-line. The key point of this method is acquiring accurate overlapped beams for synthesizing. However, the current study has two limitations. First, the scattering of light in the tissue results in the uncertain beam number of SDSOB. Thus, accurate assessments of rectal mucosal boundary (determining the relative position of the optical focus to the boundary) will be conducted to simulate the optical field distribution in the tissue based on Monte Carlo method in future works, which will lead to the best synthetic FOB. Second, the SDSOB is implemented at the cost of heavy data operations, resulting in a large image reconstruction time. This limitation may be mitigated by using high speed chips such as GPUs.

In summary, the degraded transverse resolution suffered from defocusing and scattering can be significantly improved by the SDSOB method. Unlike conventional optical-resolution PAEM, the SDSOB-PAEM possesses fine transverse resolution, high image contrast and large DOF, and may ultimately overcome the inherent tradeoff between DOF extension and resolution enhancement in optical-resolution PAEM. We demonstrated that this technology worked well for phantom and animal experiments. The SDSOB-PAEM has the potential for future clinical applications, such as the evaluation of neovascular morphology and microvessel density in tumor and inflammatory bowel disease.

References

1. J. M. Yang, C. Favazza, R. Chen, J. Yao, X. Cai, K. Maslov, Q. Zhou, K. K. Shung, and L. V. Wang, "Simultaneous functional photoacoustic and ultrasonic endoscopy of internal organs *in vivo*," Nat. Med. **18**(8), 1297–1302 (2012).

2. J. M. Yang, K. Maslov, H. C. Yang, Q. Zhou, K. K. Shung, and L. V. Wang, "Photoacoustic endoscopy," Opt. Lett. **34**(10), 1591–1593 (2009).

3. C. Chen, Y. Zhao, S. Yang, and D. Xing, "Mechanical characterization of intraluminal tissue with phase-resolved photoacoustic viscoelasticity endoscopy," Biomed. Opt. Express **6**(12), 4975–4980 (2015).

4. X. Zhu, Z. Huang, G. Wang, W. Li, D. Zou, and C. Li, "Ultrasonic detection based on polarization-dependent optical reflection," Opt. Lett. **42**(3), 439–441 (2017).

5. A. Taruttis and V. Ntziachristos, "Advances in real-time multispectral optoacoustic imaging and its applications," Nat. Photonics **9**(4), 219–227 (2015).

6. L. V. Wang and S. Hu, "Photoacoustic tomography: *in vivo* imaging from organelles to organs," Science **335**(6075), 1458–1462 (2012).

7. H. F. Zhang, K. Maslov, G. Stoica, and L. V. Wang, "Functional photoacoustic microscopy for high-resolution and noninvasive *in vivo* imaging," Nat. Biotechnol. **24**(7), 848–851 (2006).

8. J. Yao, L. Wang, J. M. Yang, K. I. Maslov, T. T. W. Wong, L. Li, C. H. Huang, J. Zou, and L. V. Wang, "High-speed label-free functional photoacoustic microscopy of mouse brain in action," Nat. Methods **12**(5), 407–410 (2015).

9. N. Wu, S. Ye, Q. Ren, and C. Li, "High-resolution dual-modality photoacoustic ocular imaging," Opt. Lett. **39**(8), 2451–2454 (2014).

10. Z. Piao, T. Ma, J. Li, M. T. Wiedmann, S. Huang, M. Yu, K. Kirk Shung, Q. Zhou, C.-S. Kim, and Z. Chen, "High speed intravascular photoacoustic imaging with fast optical parametric oscillator laser at 1.7 μm," Appl. Phys. Lett. **107**(8), 083701 (2015).

11. J. Hui, Y. Cao, Y. Zhang, A. Kole, P. Wang, G. Yu, G. Eakins, M. Sturek, W. Chen, and J.-X. Cheng, "Real-time intravascular photoacoustic-ultrasound imaging of lipid-laden plaque in human coronary artery at 16 frames per second," Sci. Rep. **7**(1), 1417 (2017).

12. K. Jansen, A. F. W. van der Steen, H. M. van Beusekom, J. W. Oosterhuis, and G. van Soest, "Intravascular photoacoustic imaging of human coronary atherosclerosis," Opt. Lett. **36**(5), 597–599 (2011).

13. J. Zhang, S. Yang, X. Ji, Q. Zhou, and D. Xing, "Characterization of lipid-rich aortic plaques by intravascular photoacoustic tomography: *ex vivo* and *in vivo* validation in a rabbit atherosclerosis model with histologic correlation," J. Am. Coll. Cardiol. **64**(4), 385–390 (2014).

14. S. Sethuraman, J. H. Amirian, S. H. Litovsky, R. W. Smalling, and S. Y. Emelianov, "Spectroscopic intravascular photoacoustic imaging to differentiate atherosclerotic plaques," Opt. Express **16**(5), 3362–3367 (2008).

15. R. Ansari, E. Z. Zhang, A. E. Desjardins, and P. C. Beard, "All-optical forward-viewing photoacoustic probe for high-resolution 3D endoscopy," Light: Sci. Appl. **7**(1), 75 (2018).

16. X. Ji, K. Xiong, S. Yang, and D. Xing, "Intravascular confocal photoacoustic endoscope with dual-element ultrasonic transducer," Opt. Express **23**(7), 9130–9136 (2015).

17. H. He, A. Buehler, D. Bozhko, X. Jian, Y. Cui, and V. Ntziachristos, "Importance of ultrawide bandwidth for optoacoustic esophagus imaging," IEEE Trans. Med. Imag. **37**(5), 1162–1167 (2018).

18. X. Bai, X. Gong, W. Hau, R. Lin, J. Zheng, C. Liu, C. Zeng, X. Zou, H. Zheng, and L. Song, "Intravascular optical-resolution photoacoustic tomography with a 1.1 mm diameter catheter," PLoS One **9**(3), e92463 (2014).

19. H. Guo, C. Song, H. Xie, and L. Xi, "Photoacoustic endomicroscopy based on a MEMS scanning mirror," Opt. Lett. **42**(22), 4615–4618 (2017).

20. J. M. Yang, R. Chen, C. Favazza, J. Yao, C. Li, Z. Hu, Q. Zhou, K. K. Shung, and L. V. Wang, "A 2.5-mm diameter probe for photoacoustic and ultrasonic endoscopy," Opt. Express **20**(21), 23944–23953 (2012).

21. J. M. Yang, C. Li, R. Chen, Q. Zhou, K. K. Shung, and L. V. Wang, "Catheter-based photoacoustic endoscope," J. Biomed. Opt. **19**(6), 066001 (2014).

22. E. Bo, Y. Luo, S. Chen, X. Liu, N. Wang, X. Ge, X. Wang, S. Chen, S. Chen, and J. Li, "Depth-of-focus extension in optical coherence tomography via multiple aperture synthesis," Optica **4**(7), 701–706 (2017).

23. J.-M. Yang, C. Li, R. Chen, B. Rao, J. Yao, C.-H. Yeh, A. Danielli, K. Maslov, Q. Zhou, K. K. Shung, and L. V. Wang, "Optical-resolution photoacoustic endomicroscopy *in vivo*," Biomed. Opt. Express **6**(3), 918–932 (2015).

24. B. Jiang, X. Yang, and Q. Luo, "Reflection-mode Bessel-beam photoacoustic microscopy for *in vivo* imaging of cerebral capillaries," Opt. Express **24**(18), 20167–20176 (2016).

25. J. Shi, L. Wang, C. Noordam, and L. V. Wang, "Bessel-beam Grueneisen relaxation photoacoustic microscopy with extended depth of field," J. Biomed. Opt. **20**(11), 116002 (2015).

26. K.-S. Lee and J. P. Rolland, "Bessel beam spectral-domain high-resolution optical coherence tomography with micro-optic axicon providing extended focusing range," Opt. Lett. **33**(15), 1696–1698 (2008).

27. K. Xiong, S. Yang, X. Li, and D. Xing, "Autofocusing optical-resolution photoacoustic endoscopy," Opt. Lett. **43**(8), 1846–1849 (2018).

28. G. Li, Z. Guo, and S.-L. Chen, "Miniature all-optical probe for large synthetic aperture photoacoustic-ultrasound imaging," Opt. Express **25**(21), 25023–25035 (2017).

29. D. Cai, G. Li, D. Xia, Z. Li, Z. Guo, and S.-L. Chen, "Synthetic aperture focusing technique for photoacoustic endoscopy," Opt. Express **25**(17), 20162–20171 (2017).

30. M.-L. Li, H. F. Zhang, K. Maslov, G. Stoica, and L. V. Wang, "Improved *in vivo* photoacoustic microscopy based on a virtual-detector concept," Opt. Lett. **31**(4), 474–476 (2006).

31. J. Turner, H. Estrada, M. Kneipp, and D. Razansky, "Improved optoacoustic microscopy through three-dimensional spatial impulse response synthetic aperture focusing technique," Opt. Lett. **39**(12), 3390–3393 (2014).

32. J. Capon, "High resolution frequency-wavenumber spectrum analysis," Proc. IEEE **57**(8), 1408–1418 (1969).
33. J. F. Synnevag, A. Austeng, and S. Holm, "Adaptive beamforming applied to medical ultrasound imaging," IEEE Trans. Ultrason. Ferroelectr. Freq. Control. **54**(8), 1606–1613 (2007).
34. S. Park, A. B. Karpiouk, S. R. Aglyamov, and S. Y. Emelianov, "Adaptive beamforming for photoacoustic imaging," Opt. Lett. **33**(12), 1291–1293 (2008).
35. M. Gu and D. Bird, "Three-dimensional optical-transfer-function analysis of fiber-optical two-photon fluorescence microscopy," J. Opt. Soc. Am. A **20**(5), 941 (2003).